SIAM J. Applied Dynamical Systems
Vol. 17, No. 2, pp. 1353–1376

Equilibrium Configurations of Boundary Droplets in a Self-Organizing Inhibitory System*

Jiajun Lu†, Frank Baginski†, and Xiaofeng Ren†

Abstract. In this paper, we study the behavior of boundary droplets in a compact domain for a self-organizing inhibitory system based on the Ohta–Kawasaki diblock copolymer theory. The free energy of the system is a sum of a local term that favors sets with boundaries that minimize perimeter and a nonlocal term related to a Green's function with Neumann boundary condition. The solutions of this system depend on the domain Ω through the Green's function, the curvature $\kappa(\xi)$ for $\xi \in \partial\Omega$, and an interaction parameter γ that multiplies the nonlocal term. The interplay between these factors influences the types of equilibria that are possible. When γ is small, a single stationary boundary droplet tends to a location $\xi_* \in \partial\Omega$ that maximizes $\kappa(\xi)$. When γ is large compared to the droplet size, the droplet tends to a location that minimizes $R_b(\xi,\xi)$ – a function related to the Green's function of the domain. In the intermediate case, the droplet locates near a point that minimizes J_b – a function involving both κ and R_b. When γ is sufficiently large, equilibrium configurations consisting of droplet assemblies exist, and we discuss the location of these droplets as well. We will focus on domains conformal to the unit disk and specifically an ellipse $\mathbb{E}_a$ with semimajor axis $a > 1$. We examine the sharp interface problem and utilize its solutions to determine the location of the boundary droplets. For an ellipse, we find R_b has two local minima co-located at the points which minimize $\kappa(\xi)$. The sharp interface theory is developed under the condition that a droplet radius is sufficiently small. To investigate droplets of moderate size, we compute finite element solutions of the diffuse interface model of the Ohta–Kawasaki equations and demonstrate that the numerical solutions of the finite element model inherit the properties exhibited by solutions of the sharp interface model. For the diffuse interface model, we consider a variety of numerical solutions, including a single droplet and assemblies with as many 20 droplets.

Key words. inhibitory system, pattern formation, conformal mapping, finite elements, optimization

AMS subject classifications. 74A50, 74G15, 35R35, 82B24, 82D60

DOI. 10.1137/17M113856X

1. Introduction.

In the Ohta–Kawasaki theory of diblock copolymers [8, 13], the density field of A-monomers is given by a function u on domain Ω, the density of B-monomers is given by $1-u$ and the free energy is

$$I(u) = \int_\Omega \left(\frac{\epsilon^2}{2}|Du|^2 + \sigma u^2(1-u)^2 \right) dA + \frac{\epsilon\gamma}{2} \int_\Omega \left((-\Delta)^{-1/2}(u-\omega) \right)^2 dA. \tag{1}$$

The parameters $\epsilon > 0, \sigma > 0$, and $\gamma \geq 0$ are related to the Flory–Huggins interaction parameter, the index of polymerization, and the molecular weight of the minority phase. See [4]

*Received by the editors July 13, 2017; accepted for publication (in revised form) by T. Warner January 25, 2018; published electronically April 26, 2018.
http://www.siam.org/journals/siads/17-2/M113856.html
Funding: The third author was supported in part by NSF grants DMS-1311856 and DMS-1714371.
†Department of Mathematics, George Washington University, Washington, DC 20052 (jjl01038@gwmail.gwu.edu, baginski@gwu.edu, ren@gwu.edu).

where a rigorous derivation of (1) can be found. In this paper, $\Omega \subset \mathbb{R}^2$ is a bounded domain, $0 < \epsilon << 1$, Du is the gradient of u, and u satisfies a mass conservation constraint

$$\fint_\Omega u dA = \omega, \quad 0 < \omega < 1, \tag{2}$$

where $\fint_\Omega u dA = |\Omega|^{-1} \int_\Omega u dA$. We define $\mathcal{A} = W^{1,2}(\Omega) \cap \left\{ \fint_\Omega u dA = \omega \right\}$ as the set of admissible functions. We refer to (1) and (2) as the *diffuse interface model.* The stationary solutions of (1) subject to (2) satisfy the corresponding Euler–Lagrange equations, a nonlinear integro-partial differential equation with constraint.

An approach that has proven to be successful in pattern formation problems has been to study the Γ-limit, $\epsilon^{-1} I \to \mathcal{J}$ as $\epsilon \to 0$, i.e.,

$$\mathcal{J}(E) = \tau P_\Omega(E) + \frac{\gamma}{2} \int_\Omega \left((-\Delta)^{-1/2} (\chi_E - \omega) \right)^2 dA, \quad E \in \Sigma, \tag{3}$$

where Σ is the collection of all measurable subsets of Ω whose measure equals $\omega|\Omega|$ and of finite perimeter, $\tau = \int_0^1 \sqrt{\sigma u^2 (1-u^2)}\, du = \sqrt{2\sigma}/6$, and $P_\Omega(E)$ is the perimeter of E (see [5, 18, 19]). The *sharp interface problem* is the problem of finding the stationary points of (3) subject to the condition $|E| = \omega|\Omega|$.

We can divide (1) by τ and redefine $\gamma' = \gamma/\tau$. This amounts to a rescaling of γ and $\mathcal{J}$. For convenience, we assume $\tau = 1$ and drop the "prime" in γ'. Asymptotic analysis and the Liapunov–Schmidt method applied to $\mathcal{J}$ for interior droplets have demonstrated the existence of a stable single droplet and stable droplet assemblies when the droplet diameter is sufficiently small. In [17], the small parameter ϵ is used to carry out perturbation analysis, and γ (an order 1 parameter) is used for bifurcation analysis to find wriggled lamellar solutions bifurcating from the perfect lamellar solutions. The existence and stability of localized patterns (spots, stripes, annuli) and periodic patterns (lamellar, hexagonal) in two dimensions are established in [10]. In one space dimension, it can be shown that the minimizers of (1) or its companion sharp interface Γ-limit problem are periodic (see, e.g., [3, 16]). Sternberg and Topaloglu have shown that for a similar problem on a flat torus, the two interface lamellar solution is stable for $0 < \gamma << 1$ and becomes unstable when γ is sufficiently large (see [21, 23]).

For an inhibitory system on a compact domain as described here, there is an energy barrier that prevents an internal droplet from drifting towards the boundary. Recently, the authors in [15] obtained analytical results for the sharp interface model when Ω is an open connected domain with C^5 boundary. One of the principal results in [15] demonstrated that a droplet could touch the boundary and that a small perturbed half-disk exists as a stable stationary set. In particular, [15, Theorem 1.2] asserts that if $\xi_* \in \partial D$ is the center of the approximate half-disk stationary set of radius ρ, then ξ_* is known asymptotically in the following three cases.

Case 1. If $\gamma << \rho^{-2}$, as $\rho \to 0$, then every limit point of ξ_* is a point that maximizes $\kappa(\xi)$.

Case 2. If $\gamma \sim \rho^{-2}$, $\gamma\rho^2 \to \beta$ as $\rho \to 0$, then every limit point of ξ_* is a minimum of

$$J_b(\xi; \beta) := -\tfrac{2}{3}\kappa(\xi) + \tfrac{1}{2}\beta(\tfrac{\pi}{2})^2 R_b(\xi, \xi).$$

Case 3. If $\gamma >> \rho^{-2}$, then for $\rho \to 0$, every limit point of ξ_* is a minimum of $R_b(\xi,\xi)$. $R_b(\xi,\xi)$ is called the *remnant function* and is related to the Green's function with Neumann boundary conditions (see (26)).

A key to establishing the results in [15] is the introduction of a generalization of a reflection operator that can be defined with respect to any sufficiently smooth boundary domain. Since we will focus on domains that are conformal to a unit disk, we can explicitly compute the Green's function with Neumann boundary conditions in terms of the fundamental solution of the Neumann problem and the conformal map without the need of introducing this generalized reflection operator. This enables us to show how features of the solutions of the inhibitory system are influenced by D. Moreover, we can utilize directly the estimates and existence results developed in [15] and [20] for the present work.

The domain $\Omega = \mathbb{E}_{a,b} = \left\{(x,y) : x^2/a^2 + y^2/b^2 \le 1\right\}$ provides an excellent benchmark for the problem defined by (1). With no loss of generality, we will assume $b^2 = a^2 - 1$ which leads to an ellipse (denoted $\mathbb{E}_a$) with foci $(\pm 1, 0)$ and semimajor axis $a > 1$. In the limiting cases, as $a \to 1^+$, $\mathbb{E}_a$ tends to a double cover of the line segment $[-1,1]$; as $a \to \infty$, $\mathbb{E}_a$ tends to a disk of infinite radius. The conformal mapping that takes $\mathbb{E}_a = \left\{(x,y) : x^2/a^2 + y^2/(a^2-1) \le 1\right\}$ to the unit disk can be expressed in terms of a Jacobi elliptic function (see Appendix A), and so we are able to explicitly calculate the Green's function with Neumann boundary conditions and the related functions, J_b and R_b.

In section 2, we discuss the construction of a Neumann function for domains conformal to a unit disk and introduce the remnant function R_b. In section 3, we present asymptotic estimates of the free energy that are needed for the analysis of the sharp interface problem. We also consider boundary droplet assemblies, but in this case, the combinatorics of possible droplet locations leads to a complicated solution set. Nevertheless, we carry out a thorough analysis of the sharp interface problem with two boundary droplets.

In order to study equilibrium configurations when the droplet size is not necessarily small or when a disk assembly has many droplets, we resort to numerical methods. A variational approach to the diffuse interface model, where ϵ is small, leads to an optimization-based interior point solution process where one directly computes the minimizers of I. In the case of the Ohta–Kawasaki model, this approach is robust and captures the features as demonstrated by the solutions of the sharp interface problem. In section 4, we present a finite element formulation of the problem:

$$\text{Problem } \mathcal{P}: \quad \inf_{u \in \mathcal{A}} I(u). \tag{4}$$

Our numerical investigations in section 4 are carried out by directly solving a discrete version of (4). We present a number of case studies and find that the numerical solutions agree qualitatively with the results predicted by the solutions of the sharp interface problem. Droplet assemblies with as many as 20 droplets are computed.

2. Green's function with Neumann boundary conditions.

In this section, we review conformal mapping theory as it applies to the solution of a boundary value problem of the second kind. We will refer to such a solution as a Green's function with Neumann boundary conditions. It is also called a Neumann function.

2.1. Conformal maps and solutions to Laplace's equation. In this section, we consider the general problem of solving the Neumann boundary value problem on a domain that can be mapped conformally onto the unit disk. This procedure is well known (see, e.g., [7, 11, 24]), and we present additional details for the convenience of the reader. To solve

$$\frac{\partial^2 u}{\partial x^2} + \frac{\partial^2 u}{\partial y^2} = 0, \quad (x, y) \in D, \tag{5}$$

with $u(x, y)$ prescribed on ∂D, let $U(\xi, \eta) = u\left(x(\xi, \eta), y(\xi, \eta)\right)$, where

$$z = f(\zeta) = x(\xi, \eta) + iy(\xi, \eta),$$

and $z = f(\zeta)$ denotes a mapping that takes a unit disk in the ζ-plane to D. We will assume that $z = f(\zeta)$ is conformal and for every $\zeta \in \mathbb{D}$, $f(\zeta) \in D$ and every point in D is of the form $f(\zeta)$ with $\zeta \in \mathbb{D}$. A similar correspondence holds for every point on ∂D and $\partial \mathbb{D}$. Furthermore, we assume that $z = f(\zeta)$ is one-to-one. It follows that

$$\frac{\partial^2 U}{\partial \xi^2} + \frac{\partial^2 U}{\partial \eta^2} = 0 \ \text{ in } \mathbb{D},$$

and U is prescribed appropriately on the boundary. Moreover, there is an analytic inverse $g(z)$ such that $f(g(z)) = z$. Note, $f(\zeta)$ is analytic, $f'(\zeta) \neq 0$, and the mapping is one-to-one. It follows that

$$u(x, y) = U(\xi, \eta) = u\left(\xi(x, y), \eta(x, y)\right) \tag{6}$$

with $g(z) = \xi(x, y) + i\eta(x, y)$ solves (5). Thus, we have solved the boundary value problem (5) via the conformal map $z = f(\zeta)$ and its conformal inverse $\zeta = g(z)$. It can be shown that this approach preserves both Dirichlet and Neumann boundary conditions (see [24, p. 243]).

2.2. Neumann functions. The Green's function of $-\Delta$ for the unit disk with Neumann boundary conditions is

$$G(\zeta, \zeta_1) = -\frac{1}{2\pi} \log|\zeta - \zeta_1| - \frac{1}{2\pi} \log|\zeta\bar{\zeta_1} - 1| + \frac{1}{2\pi}\left[\tfrac{1}{2}|\zeta|^2 + \tfrac{1}{2}|\zeta_1|^2\right] + C, \quad \zeta \neq \zeta_1 \tag{7}$$

(see, e.g., [18]). In particular, $G(\zeta, \zeta_1)$ satisfies

$$\begin{aligned} -\Delta_\zeta G(\zeta, \zeta_1) &= \delta(\zeta - \zeta_1) - \frac{1}{|\mathbb{D}|} \ \text{ in } \ \mathbb{D}, \\ \partial_n G(\zeta, \zeta_1) &= 0 \ \text{ on } \ \partial\mathbb{D}, \end{aligned}$$

where ∂_n denotes the normal derivative and $C = -3/(8\pi)$ is chosen so that

$$\frac{1}{|\mathbb{D}|} \int_{\mathbb{D}} G(\zeta, \zeta_1) dA(\zeta) = 0. \tag{8}$$

Let $\zeta = g(z)$ be a one-to-one conformal mapping from a simply connected domain D in the z-plane to the unit disk $|\zeta| < 1$. Let $z = x + iy$ and $z_1 = x_1 + iy_1$. Using the Green's

function for the unit disk with Neumann boundary conditions and the results in section 2.1, we have the Green's function for D:

$$G(z,z_1)=\frac{1}{2\pi}\left[\log\frac{1}{|g(z)-g(z_1)|}+\log\frac{1}{\left|g(z)\overline{g(z_1)}-1\right|}+\frac{|g(z)|^2}{2}+\frac{|g(z_1)|^2}{2}\right]-\frac{3}{8\pi}. \tag{9}$$

Note, (8) is replaced by the condition

$$\frac{1}{|D|}\int_D G(z,z_1)dA(z)=0$$

for all $z_1\in D$.

Consider the first term in (9) and note

$$-\frac{1}{2\pi}\log|g(z)-g(z_1)|=-\frac{1}{2\pi}\log|z-z_1|-\frac{1}{2\pi}\log\frac{g(z)-g(z_1)}{z-z_1}+\frac{1}{2\pi}i\mathrm{Arg}\frac{g(z)-g(z_1)}{z-z_1}.$$

Since the left-hand side of the last equation is real, we have

$$-\frac{1}{2\pi}\log|g(z)-g(z_1)|=-\frac{1}{2\pi}\log|z-z_1|-\frac{1}{2\pi}\mathrm{Re}\left\{\log\frac{g(z)-g(z_1)}{z-z_1}\right\}. \tag{10}$$

Considering the second term in (9), we find

$$-\frac{1}{2\pi}\log\left|g(z)\overline{g(z_1)}-1\right|=-\frac{1}{2\pi}\log\left(g(z)\overline{g(z_1)}-1\right)+\frac{i}{2\pi}\mathrm{Arg}\left(g(z)\overline{g(z_1)}-1\right).$$

Since the left-hand side of the last equation is real,

$$-\frac{1}{2\pi}\log\left|g(z)\overline{g(z_1)}-1\right|=-\frac{1}{2\pi}\mathrm{Re}\left\{\log\left(g(z)\overline{g(z_1)}-1\right)\right\}. \tag{11}$$

We define $\frac{g(z)-g(z_1)}{z-z_1}$ to be $g'(z_1)$ for $z=z_1$ so $\frac{g(z)-g(z_1)}{z-z_1}$ is analytic in D. Since $g(z)$ is one-to-one, it follows that $\frac{g(z)-g(z_1)}{z-z_1}\neq 0$. Hence, substituting (10) and (11) into (9), we find

$$G(z,z_1)=\frac{1}{2\pi}\log\frac{1}{|z-z_1|}+R(z,z_1), \tag{12}$$

where (see [24, p. 240])

$$R(z,z_1)=\frac{1}{2\pi}\mathrm{Re}\left[\log\frac{1}{g(z)\overline{g(z_1)}-1}+\log\frac{z-z_1}{g(z)-g(z_1)}\right]+\frac{|g(z)|^2}{2}+\frac{|g(z_1)|^2}{2}-\frac{3}{8\pi}. \tag{13}$$

R is the regular part of the Green's function. By construction, for every $z\in D$

$$\Delta_z R=-\frac{1}{|D|}\quad\text{for all}\quad z_1\in D,$$
$$\partial_n R=\partial_n\left(\frac{1}{2\pi}\log|z-z_1|\right),\quad z_1\in\partial D.$$

2.3. Remnant function R_b. In general, the Green's function $G(z,w)$ of $-\Delta$ on D with the Neumann boundary condition is the sum of two parts:

$$G(z,w) = \frac{1}{2\pi}\log\frac{1}{|z-w|} + R(z,w), \tag{14}$$

where the first term is the fundamental solution of the $-\Delta$ operator, and the second term R is the regular part of G, a smooth function on $D\times D$. It is known that

$$R(z,w)\to\infty \quad \text{if } z\to p,\ w\to p, \text{ and } p\in\partial D. \tag{15}$$

It is important to know how R blows up in (15). We create a reflection operation about the boundary of D. This reflection operation, denoted by $z\to\tilde{z}$, is defined for all z in a neighborhood of ∂D.

In the case that D has analytic boundary, one may take $\tilde{z}$ to be the Schwarz reflection of z. Let h be a bijective analytic function that maps D to the upper half of the complex plane $\mathbb{C}$, and maps ∂D to the real axis of $\mathbb{C}$. Then

$$\tilde{z} = h^{-1}(\overline{h(z)}), \tag{16}$$

where the overline denotes complex conjugation.

Another way to do Schwarz reflection is by the inversion operation. Recall that inversion about the unit disc $\mathbb{D}=\{\zeta\in\mathbb{C}:\ |\zeta|\le 1\}$ is

$$\zeta\to\zeta^* = 1/\overline{\zeta}. \tag{17}$$

Let g be a bijective analytic function that maps D to $\mathbb{D}$. Then

$$\tilde{z} = g^{-1}((g(z))^*). \tag{18}$$

With the reflection operation, the regular part $R(z,w)$ of the Green's function can itself be decomposed into two parts:

$$R(z,w) = \frac{1}{2\pi}\log\frac{1}{|z-\tilde{w}|} + R_b(z,w), \tag{19}$$

defined for $z\in\overline{D}$ and $w\in D_\delta$, where D_δ is an open set consisting of points in D that are δ-close to ∂D. The function R_b is smooth up to the boundary of D; one can extend the domain of $R_b(z,w)$ to $(z,w)\in\overline{D}\times\overline{D_\delta}$. In particular, $R_b(z,z)$ is well defined for $z\in\partial D$. The blowup behavior in (15) is caused by the first term of (19). With $z,w\in D$, $z\to p$, $w\to p$, and $p\in\partial D$, $R_b(z,w)\to R_b(p,p)$ but $\frac{1}{2\pi}\log\frac{1}{|z-\tilde{w}|}$ blows up as z and $\tilde{w}$ approach p.

The results in our work are dependent on $R_b(p,p)$ for $p\in\partial D$, instead of the whole function $R_b(z,w)$ for $(z,w)\in\overline{D}\times\overline{D_\delta}$. By (19) we see that

$$R_b(p,p) = \lim_{w\to p}\left(R(p,w) - \frac{1}{2\pi}\log\frac{1}{|p-w|}\right),\ p\in\partial D. \tag{20}$$

Here we can replace $\tilde{w}$ by w because $p\in\partial D$.

Let us illustrate the above construction for the case $D = \mathbb{D}$. From (7), we have

$$G(z,w) = \frac{1}{2\pi}\log\frac{1}{|z-w|} + \frac{1}{2\pi}\left[\frac{|z|^2}{2} + \frac{|w|^2}{2} + \log\frac{1}{|z\overline{w}-1|}\right] - \frac{3}{8\pi} \tag{21}$$

and

$$R(z,w) = \frac{1}{2\pi}\left[\frac{|z|^2}{2} + \frac{|w|^2}{2} + \log\frac{1}{|z\overline{w}-1|}\right] - \frac{3}{8\pi}. \tag{22}$$

One can see that $R(z,w) \to \infty$ if $z, w \to p \in \partial D$ because of the log term.

By (19), and since $\tilde{w} = w^* = 1/\overline{w}$ in this case,

$$\begin{aligned} R_b(z,w) &= R(z,w) - \frac{1}{2\pi}\log\frac{1}{|z-w^*|} \\ &= \frac{1}{2\pi}\left[\frac{|z|^2}{2} + \frac{|w|^2}{2} + \log\frac{1}{|z\overline{w}-1|}\right] - \frac{3}{8\pi} - \frac{1}{2\pi}\log\frac{|\overline{w}|}{|z\overline{w}-1|} \\ &= \frac{1}{2\pi}\left[\frac{|z|^2}{2} + \frac{|w|^2}{2}\right] - \frac{3}{8\pi} - \frac{1}{2\pi}\log|w|. \end{aligned}$$

Note that R_b is smooth on $\overline{D} \times \overline{D_\delta}$. The only singularity occurs at $w = 0$, but this point is far away from the boundary of D. Finally we can take $z = w = p \in \partial D$ in $R_b(z,w)$ and find

$$R_b(p,p) = \frac{1}{8\pi},\ p \in \partial D, \tag{23}$$

which is a constant in this case.

For the case of the ellipse, we define $R_b(z,w)$ as follows:

$$\begin{aligned} R_b(z,w) &= R(z,w) - \frac{1}{2\pi}\mathrm{Re}\left\{\log\frac{1}{g(z)-g(\tilde{w})}\right\} \\ &= \frac{1}{2\pi}\mathrm{Re}\left\{\log\frac{1}{\left[g(z)\overline{g(w)}-1\right]}\frac{1/\overline{g(w)}}{1/\overline{g(w)}} + \log\frac{z-w}{g(z)-g(w)} + \frac{1}{2}\left[|g(z)|^2 + |g(w)|^2\right]\right. \\ &\quad \left. - \frac{1}{2\pi}\log\frac{1}{g(z)-g(\tilde{w})}\right\} - \frac{3}{8\pi} \\ &= \frac{1}{2\pi}\mathrm{Re}\left\{\log\frac{1}{\overline{g(w)}} + \log\frac{z-w}{g(z)-g(w)} + \frac{1}{2}\left[|g(z)|^2 + |g(w)|^2\right]\right. \\ &\quad \left. + \log\frac{g(z)-g(\tilde{w})}{g(z)-1/\overline{g(w)}}\right\} - \frac{3}{8\pi}. \end{aligned}$$

For $w = p \in \partial D$, it follows that $g(p) \in \partial\mathbb{D}$, $|g(p)| = 1$, $g(\tilde{p}) = 1/\overline{g(p)}$, and

$$R_b(z,p) = \frac{1}{2\pi}\mathrm{Re}\left\{\log\frac{z-p}{g(z)-g(p)} + \frac{1}{2}\left[|g(z)|^2 + |g(p)|^2\right]\right\} - \frac{3}{8\pi}.$$

Finally, if $z \to p \in \partial D$, we find

$$R_b(p,p) = \frac{1}{8\pi} + \frac{1}{2\pi}\mathrm{Re}\left\{\log\frac{1}{g'(p)}\right\}. \tag{24}$$

At times, it will be convenient to write $R_b = R_b(u,u)$, where u is described in (48).

The Green's function for $D = \mathbb{E}_a$ is defined by (12) and (13) with

$$g(z) = \left(\sqrt[4]{s}\right)\mathrm{sn}\left(\left(\frac{2K}{\pi}\arcsin z\right)\middle| s\right) \quad \text{for } z \in \mathbb{E}_a,$$

where $\mathrm{sn}(\cdot|s)$ is the Jacobi elliptic function of modulus s (see (44) in Appendix A where s is defined and its relation to a is discussed). For economy of space, s can be omitted when its definition is clear from the context. R_b is defined by (24) with

$$g'(z) = \frac{2K}{\pi}\left(\sqrt[4]{s}\right)\mathrm{cn}\left(\frac{2K}{\pi}\arcsin z\right)\mathrm{dn}\left(\frac{2K}{\pi}\arcsin z\right)\frac{1}{\sqrt{1-z^2}}.$$

In particular, we have

$$\begin{aligned} G(z,w) = \frac{1}{2\pi}\Bigg\{ &\log\frac{1}{\left|\sqrt[4]{s}\left[\mathrm{sn}\left(\frac{2K}{\pi}\arcsin z\right) - \mathrm{sn}\left(\frac{2K}{\pi}\arcsin w\right)\right]\right|} \\ &+ \log\frac{1}{\left|\left(\sqrt[2]{s}\right)\mathrm{sn}\left(\frac{2K}{\pi}\arcsin z\right)\overline{\mathrm{sn}\left(\frac{2K}{\pi}\arcsin w\right)} - 1\right|} \\ &+ \frac{\sqrt{s}}{2}\left[\left|\mathrm{sn}\left(\frac{2K}{\pi}\arcsin z\right)\right|^2 + \left|\mathrm{sn}\left(\frac{2K}{\pi}\arcsin w\right)\right|^2\right]\Bigg\} - \frac{3}{8\pi} \end{aligned} \tag{25}$$

and

$$R_b(p,p) = \frac{1}{8\pi} + \frac{1}{2\pi}\left\{\log\frac{1}{\left|\frac{2K}{\pi}\left(\sqrt[4]{s}\right)\mathrm{cn}\left(\frac{2K}{\pi}\arcsin z\right)\mathrm{dn}\left(\frac{2K}{\pi}\arcsin z\right)/\sqrt{1-z^2}\right|}\right\}. \tag{26}$$

As we shall see, $R_b(p,p)$ for $p \in \partial\mathbb{E}_a$ has two energy wells which coincide with the minima of $\kappa(p)$.

Note that $z = \pm 1 \notin \partial\mathbb{E}_a$ for $a > 1$. Moreover, $g'(\pm 1)$ can be defined through a limiting process. As $z \to 1$, $\arcsin(z) \to \frac{1}{2}\pi$ and we find

$$\begin{aligned} \lim_{z\to 1}\mathrm{dn}\left(\frac{2K}{\pi}\arcsin z\right) &= \sqrt{1-s}, \\ \lim_{z\to 1}\frac{\mathrm{cn}\left(\frac{2K}{\pi}\arcsin z\right)}{(1-z^2)^{1/2}} &= \frac{2K}{\pi}\sqrt{1-s}. \end{aligned}$$

Similar results hold for $z \to -1$ and it follows that

$$g'(\pm 1) = \left(\frac{2K}{\pi}\right)^2 s^{1/4}(1-s).$$

3. Asymptotics. Stationary solutions of the related Γ-limit problem provide some clues about droplet distribution at equilibrium. The density function u in (1) approximates the indicator function for set E in (3), i.e., $(u \approx \chi_E)$. Moreover, since $\epsilon^{-1} I \to \mathcal{J}$ as $\epsilon \to 0$, a sharp interface solution provides a good initial seed for the finite element method discussed in section 4. For the convenience of the reader, we summarize a number of asymptotic estimates that are relevant to the sharp interface analysis and refer to [15] and [20] for detailed derivations. For a single droplet of radius ρ, there are three energy estimates corresponding to how γ compares with ρ^{-2}. Although [20] discusses assemblies with interior and boundary droplets (similar in nature to to the solutions of the Coulombic repulsion problem discussed in [12]), we focus our attention on boundary droplet assemblies in this paper.

3.1. Energy of a single boundary half-disk. The total energy of a stationary boundary half-disk of radius ρ centered at $\xi \in \partial D$ is (see [15, Lemma 2.3])

$$\mathcal{J}(E) = \pi\rho - \frac{2\rho^2\kappa(\xi)}{3} + O(\rho^3) + \frac{\gamma}{2}\left(\frac{\pi\rho^4}{4}\log\frac{1}{\rho} + \frac{\pi\rho^4}{16} + \left(\frac{\pi\rho^2}{2}\right)^2 R_b(\xi,\xi) + O(\rho^5)\right), \tag{27}$$

where $\kappa(\xi)$ is the boundary curvature at $\xi \in \partial D$. If $0 < \gamma << \rho^{-2}$, then it follows that

$$\mathcal{J}(E) = \pi\rho - \frac{2\rho^2\kappa(\xi)}{3} + \frac{\gamma}{2}\left(\frac{\pi\rho^4}{4}\log\left(\frac{1}{\rho}\right)\right) + o(\rho^2)$$

and $\mathcal{J}(E)$ is minimized when $\kappa(\xi)$ is maximized.

In the case $\gamma \sim \frac{1}{\rho^2}$ and $\gamma\rho^2 \to \beta$ as $\rho \to 0$, we find

$$\mathcal{J}(E) = \pi\rho - \frac{2\rho^2\kappa(\xi)}{3} + \frac{\gamma}{2}\left(\frac{\pi\rho^4}{4}\log\frac{1}{\rho} + \frac{\pi\rho^4}{16}\right) + \frac{\rho^2\beta}{2}\left(\frac{\pi}{2}\right)^2 R_b(\xi,\xi) + o(\rho^2). \tag{28}$$

It follows that $\mathcal{J}(E)$ is minimized when ξ converges to a minimum of

$$J_b(\xi,\beta) := -\frac{2}{3}\kappa(\xi) + \tfrac{1}{2}\beta\left(\frac{\pi}{2}\right)^2 R_b(\xi,\xi). \tag{29}$$

To be consistent with [15], we use β to denote the limit of $\gamma\rho^2$.

If $\gamma >> \rho^{-2}$ is large and $\gamma\rho^3$ is bounded, then the energy of a boundary droplet is

$$\mathcal{J}(E) = \pi\rho + \frac{\gamma}{2}\left(\frac{\pi\rho^4}{4}\log\frac{1}{\rho} + \frac{\pi\rho^4}{16}\right) + \frac{\gamma\rho^4}{2}\left(\frac{\pi}{2}\right)^2 R_b(\xi,\xi) + O(\rho^2).$$

The terms of order $O(\rho^2)$ can be ignored and $\mathcal{J}(E)$ is minimized when $R_b(\xi,\xi)$ is minimized; i.e., ξ tends to a minimum of $R_b(\xi,\xi)$.

3.2. Energy of an assembly of boundary droplets. Following the notation in [20], we let $\rho_b^j > 0$ be the radius of a half-disk centered at $\xi_b^j \in \partial D$ for $j = 1, 2, \ldots, n_b$, i.e.,

$$E_b^j = \left\{ z \in D : |z - \xi_b^j| < \rho_b^j \right\}.$$

A boundary disk assembly is denoted

$$E = \cup_{j=1}^{n_b} E_b^j.$$

When γ is sufficiently large, the first integral in (1) is approximately the total perimeter of all the boundary half-disks and the total energy of a stationary disk assembly E is given by (see [20, Lemma 29])

$$\begin{aligned} \mathcal{J}(E) = &\sum_{j=1}^{n_b} \pi \rho_b^j + O(\rho^2) \\ &+ \frac{\gamma}{2} \left[\sum_{j=1}^{n_b} \frac{\pi(\rho_b^j)^4}{4} \log \frac{1}{\rho_b^j} + \frac{\pi(\rho_b^j)^4}{16} + \left(\frac{\pi(\rho_b^j)^2}{2} \right)^2 R_b(\xi_b^j, \xi_b^j) \right. \\ &\left. + \sum_{j=1}^{n_b} \sum_{k=j+1}^{n_b} \left(\frac{(\pi \rho_b^j)^2}{2} \right) \left(\frac{(\pi \rho_b^k)^2}{2} \right) G(\xi_b^j, \xi_b^k) \right] + O(\gamma \rho^5). \end{aligned} \tag{30}$$

3.3. Case studies. Before proceeding to the analysis of the ellipse, it is important to note how R_b depends on the shape of the domain and specifically how it depends on the conformal parameter a. In Figure 1, we present graphs of $\kappa(u)$ and $R_b(u, u)$ for a number of a's. Recall $K = \mathsf{K}(s^2)$, but s depends on a through (43). In order to distinguish the critical points of both κ and R_b, we superpose them using two different ordinate axis scales. In Figure 1, the units on the left ordinate axis are with respect to $\kappa(u)$; the units on the right ordinate axis are with respect to $R_b(u, u)$. Note that for all $a > 1$, $R_b(u, u)$ has two wells located at the points where κ is a minimum.

3.3.1. Single boundary droplet. For a single droplet with γ small, we see from Figure 1 and section 3.1 that $\mathcal{J}$ is minimized when κ is maximized (Case 1). In this case, the droplet locates near $\xi = \pm a + 0i$. On the other hand, when γ is large, Figure 1 and section 3.2 suggest that $\mathcal{J}$ is minimized when R_b is minimized (Case 3) and the droplet locates near $\xi = 0 \pm i$.

To illustrate single droplet behavior in $\mathbb{E}_a$ in Case 2, we consider $a = \sqrt{2}$. To set a scale, we considered a droplet of size $\rho \approx 0.1$ and $\beta \approx 4$. For the case $\gamma << \rho^{-2}$ and $\gamma \rho^2 \to \beta$, J_b can posses either two or four wells based on the value of β (see Figure 2).

3.3.2. Two boundary droplets. In the following section, we suppose $\gamma >> \frac{1}{\rho^2}$ and there are two boundary droplets (Droplets 1 and 2) located at $u = u_1$ and $u = u_2$, respectively. We can express the energy of the sharp interface problem as $\mathcal{J} = \mathcal{J}(u_1, u_2)$ using (30) and ignoring the terms $O(\gamma \rho^5)$. We found the graphics easier to visualize if we considered $u_i \in [0, 4K]$ (instead of $[-K, 3K]$ as was used previously). In Figure 3(a), we present the graph of $\mathcal{J}$ for $a = \sqrt{2}$. The level sets of $\mathcal{J}$ are presented in Figure 3(b). After a careful examination of

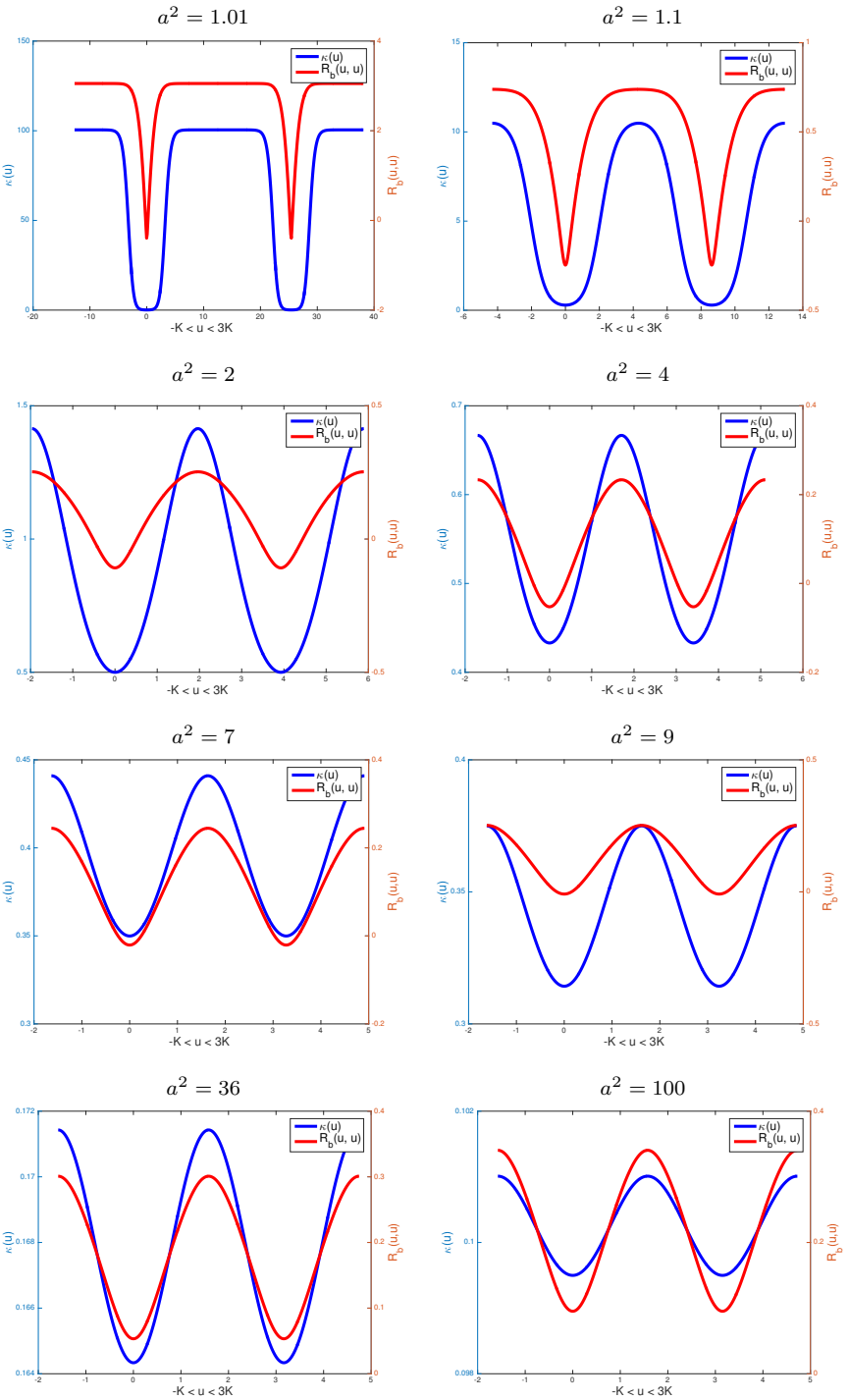

Figure 1. $R_b(u,u)$, $\kappa(u)$ *for* $-K < u < 3K$ *and* $1 < a < 10$.

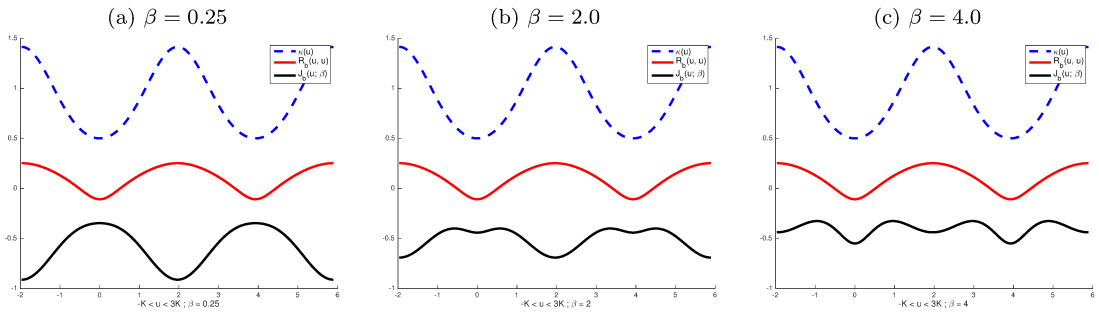

Figure 2. *$J_b(u;\beta)$ for $-K < u < 3K$, $a^2 = 2$, $\gamma\rho^2 \to \beta$.*

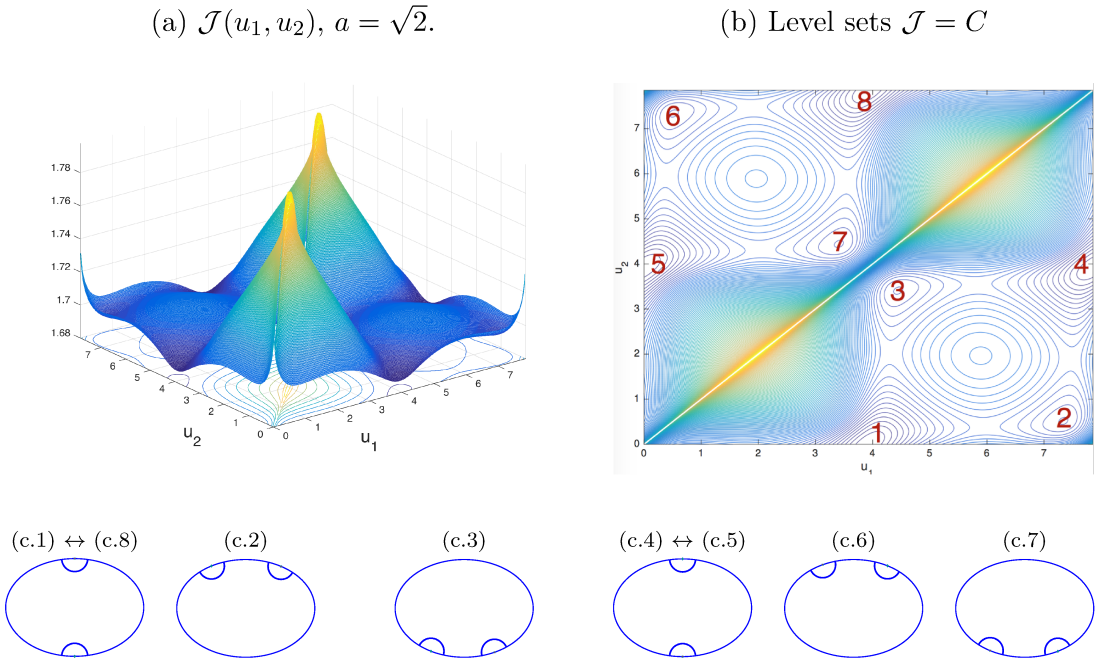

Figure 3. *Two boundary droplets in an ellipse with $a = \sqrt{2}$.*

the level sets, we determined there were a total of eight local minima which are enumerated in Figure 3(b). The droplets corresponding to these respective local minima are presented in Figure 3(c.1)–(c.8). Note that because $z(u,0) = z(u,4K)$ and $z(0,u) = z(4K,u)$, Critical points 1 and 8 and critical points 4 and 5 represent the same respective boundary points. If we use the fact that $\mathcal{J}$ is symmetric, i.e., $\mathcal{J}(u_1,u_2) = \mathcal{J}(u_2,u_1)$ and do not label the droplets, we find there are three distinct two-droplet assemblies.

Next, we consider $\mathbb{E}_9$ and find a total of six two-droplet assemblies as shown in Figure 4. In this case, $a = 9$, $b = 8.94$, and the ellipse is nearly a disk. If we ignore labeling the droplets, there are three distinct two-droplet assemblies in this case.

Next, we consider $\mathbb{E}_3$ and find a total of eight two-droplet assemblies, as shown in Figure 5. In this case, $a = 3$, $b = 2.83$, and the ellipse is nearly a circle in this case as well. If we ignore labeling the droplets, there are four distinct two-droplet assemblies in this case.

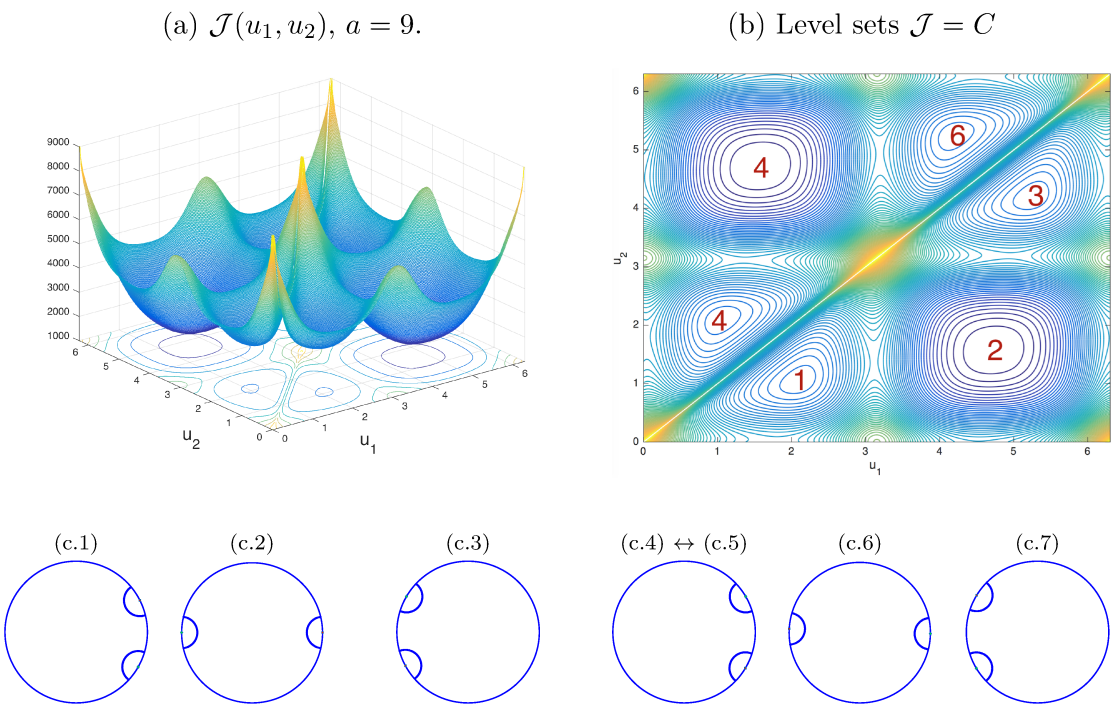

Figure 4. *Two boundary droplets in an ellipse with* $a = 9$.

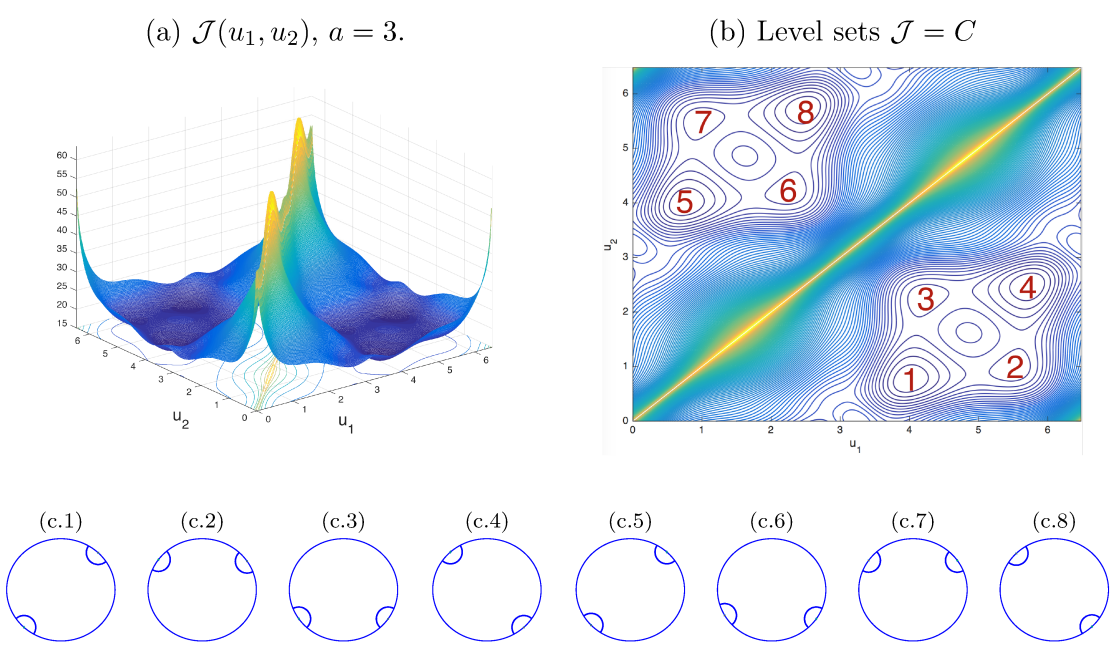

Figure 5. *Two boundary droplets in an ellipse with* $a = 3$.

4. Finite element model. In the following, we suppose that $\epsilon > 0, \sigma > 0$, and $\gamma \geq 0$ are fixed and Ω is a domain conformal to the unit disk.

4.1. Otha–Kawasaki finite element model. Let $C^1_{pw}(\Omega;\mathbb{R})$ denote the set of piecewise continuously differentiable functions $u : \Omega \to \mathbb{R}$. $\mathcal{H}(\Omega)$ denotes the Hilbert space $W^{1,2}(\Omega)$, the completion of $C^1_{pw}(\Omega;\mathbb{R})$ with respect to

$$||u||^2_{1,2} = \int_\Omega \left(|Du|^2 + u^2\right) dA.$$

$\mathcal{V}(\Omega)$ is the completion of $\{v \in C^2(\Omega;\mathbb{R}) \cap C^1(\bar{\Omega};\mathbb{R}), \partial_n v = 0 \text{ on } \partial\Omega\}$ with respect to

$$||v||^2_{2,2} = \int_\Omega \left(|\Delta v|^2 + |Dv|^2 + v^2\right) dA.$$

$\mathcal{V}(\Omega)$ is a closed subspace of $W^{2,2}(\Omega)$.

It will be convenient to rewrite (1) in a form that lends itself to numerics. With this in mind, we define v to be a solution of the Neumann problem:

$$\begin{aligned} -\Delta v(x) &= u(x) - \omega, && x \in \Omega, \\ \partial_n v &= 0, && x \in \partial\Omega, \\ \int_\Omega v dA &= 0. \end{aligned} \tag{31}$$

The third condition in (31) holds because $\fint_\Omega u \, dA = \omega$, where $0 < \omega < 1$. It follows that $v = (-\Delta)^{-1}(u - \omega)$. Formally, $(-\Delta)^{-1}$ is an integral operator expressed in terms of a Green's function (see [2]). Using Green's identity, we can rewrite the second integral in (1) as

$$\begin{aligned} \int_\Omega \left((-\Delta)^{-\frac{1}{2}}(u-\omega)\right)^2 dA &= \int_\Omega \left[(-\Delta)^{-1}(u-\omega)\right](u-\omega) dA \\ &= \int_\Omega v(-\Delta v) dA \\ &= \int_\Omega |Dv|^2 dA. \end{aligned}$$

With $W(u) = u^2(1-u)^2$, the free energy can be expressed as

$$I(u) = \int_\Omega \left\{ \tfrac{1}{2}\epsilon^2 |Du|^2 + \sigma W(u) + \tfrac{1}{2}\epsilon\gamma |Dv|^2 \right\} \, dA, \tag{32}$$

which, as we shall see, lends itself well to the computation of numerical minimizers.

For future reference, we record the weak formulation of (31): Given a fixed $u \in \mathcal{H}(\Omega)$ and $0 < \omega < 1$, find $v \in \mathcal{V}(\Omega)$ such that

$$a(v,\phi) = (u - \omega, \phi) \quad \text{for all} \quad \phi \in \mathcal{H}(\Omega),$$

$$\begin{aligned} a(u,\phi) &= \int_\Omega Du \cdot D\phi dA, \\ (u-\omega,\phi) &= \int_\Omega (u-\omega)\phi dA, \end{aligned} \tag{33}$$

and $(u,\phi) = \int_\Omega u\phi dA$ is the usual inner product on $L^2(\Omega)$.

We will follow the usual finite element approach to discretizing (4) (see, e.g., [9]). To insure an accurate finite element solution, the meshes for triangular discretization used in our numerical calculations are generated by Persson's mesh generator [14] which produces high-quality meshes consisting of triangles that are almost equilateral. This is a desirable property when solving PDEs with the finite element method. Upper bounds on the errors depend only on the smallest angle in the mesh, and if all angles are close to 60°, good numerical results are achievable. A mesh of an ellipse with $(a, b) = (\sqrt{2}, 1)$ and $h = 0.086$ is shown in Figure 6(a). A typical triangle τ is shown in Figure 6(b). Let Ω_h be a triangulation of Ω with positive orientation, i.e., $\Omega_h = \cup_{j=1}^{N_T} \tau_j$, where τ_j denotes a typical triangle and N_T is the number of triangles in Ω_h. Let $P = \{P_1, P_2, \ldots, P_N\}$ denote the vertices in the triangulation Ω_h, where h is the average edge length of the triangles. In Table 1, we present a summary of the meshes used in our calculations. Typically, $\epsilon \approx \frac{1}{2}h$ produced reasonable results. We will use the terms coarse, medium, fine, and ultrafine when referring to meshes with $h \approx 0.08$, 0.04, 0.02, and 0.01, respectively. With an unstructured grid, we found that the computation time was long with an ultrafine mesh, but a medium to fine grid was sufficient to capture the important features characterizing the patterns in the solutions at the respective scales. From a practical standpoint, if the features in a pattern are too fine, a coarse mesh will not be able to capture those features. In this case, the solution process terminates with the solver evolving a constant solution. However, if h is chosen to be at the proper scale when compared with the features of the patterns of interest, then a medium grid will suffice.

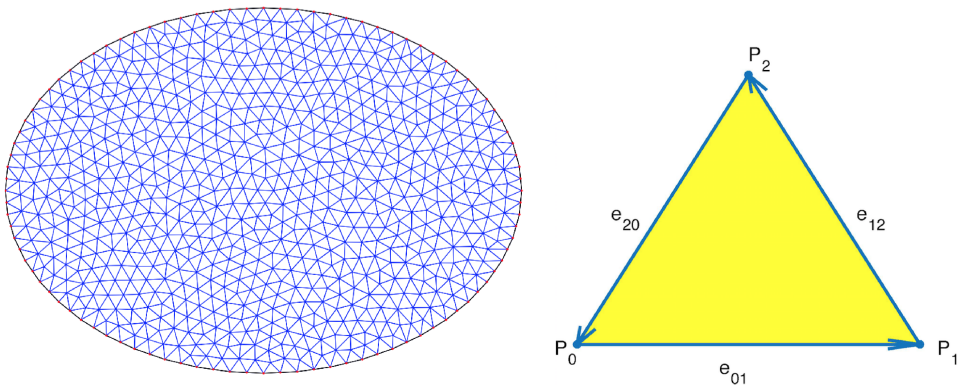

(a) Mesh $(N, N_T) = (746, 1, 394)$. (b) Triangle τ, positively oriented.

Figure 6. (a) *A triangulation of* $x^2/2 + y^2 = 1$, $h = 0.086$*;* (b) *typical triangle* $\tau \in \Omega_h$.

Table 1
Mesh statistics.

Grid	h	N	N_T
Coarse	0.0861	746	1,394
Medium	0.0435	2,828	5,462
Fine	0.0217	11,112	21,838
Ultrafine	0.0109	44,050	87,330

Let P_0, P_1, and P_2 denote vertices in a typical triangle τ. The vertices are positively oriented so that $\mathbf{e_{01}} = P_1 - P_0$, $\mathbf{e_{12}} = P_2 - P_1$, $\mathbf{e_{20}} = P_0 - P_2$, and $\mathbf{e_{01}} \times \mathbf{e_{12}}$ is the outer normal to Ω_h. In our discretization, the geometry is fixed and the degrees of freedom are the values of the phase function u at vertices P_i for $i = 1, \ldots, N$. There should be no confusion between elements of the set $\{P_0, P_1, P_2\}$ denoting vertices of a generic triangle τ and elements of the set $\{P_1, P_2, P_3, \ldots, P_N\}$ denoting vertices of the triangulation Ω_h.

A finite element solution is sought in the finite dimensional space

$$S_h = \{\varphi_h \in \mathcal{A}, \varphi_h \text{ linear on } \tau_j\},$$

where by linear we mean a function of the form $w(x, y, z) = a + bx + cy + dz$ for $(x, y, z) \in \tau_j$. When $a \neq 0$, such a function is said to be affine. Let $P_j = (x_j, y_j, z_j)$ and define $\Phi_i(x, y, z)$ so that

$$\Phi_i(P_j) = \begin{cases} 1, & i = j, \\ 0, & i \neq j, \end{cases} \quad 1 \leq i, j \leq N,$$

where $\{\Phi_i : i = 1, \ldots, N\}$ is a set of basis functions. Hence, any $v_h \in S_h$ can be written as

$$v_h(x, y, z) = \sum_{j=1}^{N} v_j \Phi_j(x, y, z),$$

where $v_j = v(P_j)$. The finite dimensional version of (31) is to find $v_h \in S_h$ such that

$$\begin{aligned} &a(v_h, \psi) = (u_h - \omega, \psi) \quad \text{for all } \psi \in S_h, \\ &\int_{\Omega_h} v_h dA = 0, \end{aligned} \tag{34}$$

where $a(v, \psi)$ is defined in (33) and the last equation in (34) is the discrete version of the mass constraint. Expressing v_h in terms of the basis functions $\{\Phi_j, j = 1, \ldots, N\}$ and then inserting into (34), we are led to the linear system

$$\sum_{j=1}^{N} v_j a(\Phi_j, \Phi_i) = (u_h - \omega, \Phi_i), \quad i = 1, \ldots, N, \tag{35}$$

$$\sum_{j=1}^{N} \int_{\Omega_h} v_j \Phi_j \, dA = 0. \tag{36}$$

The first N equations (35) can be written in the form $AV = F$, where $A = (a_{ij}) = a(\Phi_j, \Phi_i)$ is the $N \times N$ stiffness matrix and $F \in \mathbb{R}^N$ is the forcing term. If we augment the matrix A by appending a row derived from (36) and appending a zero to F, we are led to a matrix equation $\tilde{A}V = \tilde{F}$, where $\tilde{A}$ is $(N + 1) \times N$ and $\tilde{F} \in \mathbb{R}^{N+1}$ ($\tilde{F}_{N+1} = 0$). The rank of $\tilde{A}$ is N, so we form

$$\tilde{A}^T \tilde{A} V = \tilde{A}^T \tilde{F}, \text{ where } V = (v_1, \ldots, v_N)^T. \tag{37}$$

Note, for fixed $0 < \omega < 1$, the solution of (37) is unique. Thus,

$$V = \begin{bmatrix} v_1 \\ v_2 \\ \vdots \\ v_N \end{bmatrix} = \left(\tilde{A}^T \tilde{A}\right)^{-1} \tilde{A}^T \begin{bmatrix} (u_1 - \omega, \Phi_1) \\ (u_2 - \omega, \Phi_2) \\ \vdots \\ (u_N - \omega, \Phi_N) \\ 0 \end{bmatrix}. \tag{38}$$

A function $u \in \mathcal{H}(\Omega)$ is approximated by a $u_h \in S_h$, i.e.,

$$u_h(x, y, z) = \sum_{j=1}^{N} u_j \Phi_j(x, y, z),$$

where $u_j = u(P_j)$. The *linear* mass constraint $\int_{\Omega_h} u_h dA = \omega$ is included in the definition of $\mathcal{A}$ of feasible solutions. The mass constraint can be written in the form of

$$A_{eq} U = \omega |\Omega| \quad \text{for some } N \times 1 \text{ matrix } A_{eq}. \tag{39}$$

It follows that

$$\int_{\Omega} |Du|^2 dA \approx \int_{\Omega_h} |Du_h|^2 dA = U^T A U$$

and

$$\int_{\Omega} |Dv|^2 dA \approx \int_{\Omega_h} |Dv_h|^2 dA = V^T A V,$$

where V is given by (38). For the second term in $I(u)$, we have

$$\int_{\Omega} u^2 (1-u)^2 \, dA \approx \int_{\Omega_h} u_h^2 (1-u_h)^2 \, dA = N(U), \quad u \in \mathcal{H}(\Omega),$$

where the integration over Ω_h is carried out exactly for the piecewise linear function u_h, leading to the nonlinear functional $N(U) : \mathbb{R}^N \to \mathbb{R}$.

We are lead to the discrete version of (4),

$$\text{Problem } \mathcal{P}_h: \quad \inf_{U \in \mathbb{R}^N, A_{eq} U = \omega |\Omega|} I^h(U), \tag{40}$$

where $I^h(U) = \frac{1}{2}\epsilon^2 U^T A U + \sigma N(U) + \frac{1}{2}\gamma\epsilon V^T A V$ and V denotes the unique solution of (38).

We say a solution U^* (or u_h^*) of Problem $\mathcal{P}_h$ is stable in S_h if the Hessian matrix

$$H^* = H(U^*) = \left[\frac{\partial^2 I^h(U^*)}{\partial u_i \partial u_j}\right]_{1 \le i,j \le N}$$

is positive definite, i.e., all eigenvalues of H^* are positive. We say that a solution U^* of Problem $\mathcal{P}_h$ is unstable in S_h if at least one eigenvalue is negative. Otherwise, we say that the stability in S_h is indeterminate. An equivalent way of saying this is *a solution U^* is stable in S_h* if

$$\inf_{||U|| \neq 0} \frac{1}{2} U^T H^* U > 0$$

for $U = U^* + \delta U$ and $|\delta U|$ sufficiently small.

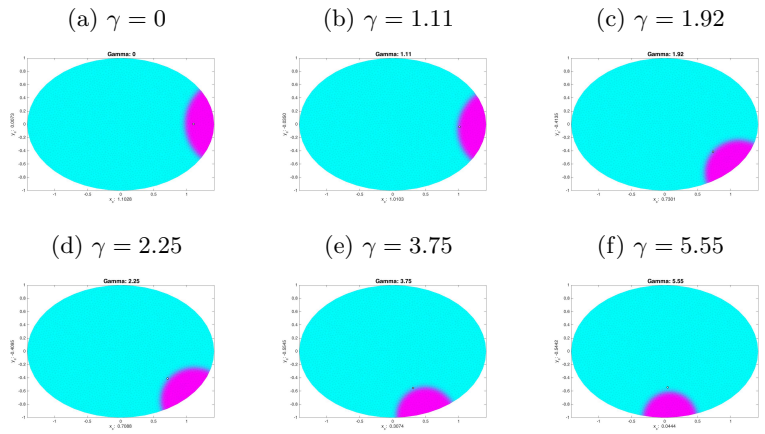

Figure 7. *Single boundary droplet solutions.*

Table 2
Single boundary droplet data for intermediate values of γ; $\rho = 0.46$, $\rho^{-2} = 4.73$.

Figure	γ	ρ^{-2}	$\gamma\rho^2$	Case
7(a)	0	4.73	0.00	$\gamma \ll \rho^{-2}$
7(b)	1.11	4.73	0.235	$\gamma \ll \rho^{-2}$
7(c)	1.92	4.73	0.406	$\gamma \sim \rho^{-2}$
7(d)	2.25	4.73	0.476	$\gamma \sim \rho^{-2}$
7(e)	3.75	4.73	0.793	$\gamma \gg \rho^{-2}$
7(f)	5.55	4.73	1.174	$\gamma \gg \rho^{-2}$

4.2. Numerical results.

4.2.1. Single boundary droplet. Consider $\mathbb{E}_{\sqrt{2}}$ and suppose $\omega = 0.075$. Figure 7(a)–(f) shows a boundary droplet moving from $z = \sqrt{2} + 0i$ to $z = 0 - i$ as γ varies from 0 to 5.5. These results are consistent with Cases 1–3 presented in section 1 and the analysis of the R_b-function presented in section 3. See Table 2, where the values of γ need to be divided by τ when comparing with the sharp interface model. When γ is zero or small, a boundary droplet locates itself at a point of maximum curvature (Figure 7(a) and (b)). As γ increases, the R_b-function and its interaction with the curvature of the boundary determine the location of the droplet which moves along the boundary toward $z = 0 - i$, as shown in Figure 7(c)–(e). As γ increases further, the center of the droplet moves closer to $0 - i$ but never quite gets there. This is not unexpected, since the long- and short-range terms will continue to counterbalance one another. The "pull" of the short-range term will always prevent the droplet from centering at $0 - i$. This type of interaction also explains why a single droplet numerical solution does not center precisely at one of the wells described in Figures 1 and 2 when $\gamma > 0$. In our numerical model, a further increase in γ will cause the droplet to disintegrate and the numerical solution will converge to a constant. The sharp interface model assumes ρ is small, and the analysis does not offer precise estimates for parameter ranges in the three single droplet cases discussed in section 3. Nevertheless, the numerical computations presented for the solutions of (4) are

consistent with the predictions based on the sharp interface model for a single droplet. All numerical solutions were found to be stable in S_h.

4.2.2. Boundary droplet assemblies. In section 3.3.2, we considered the sharp interface problem for boundary droplet assemblies. Based on the droplet position predicted by the sharp interface model, it was not difficult to place two, three, or four droplets of approximately the same size and have the numerical solution of (40) converge. For the solutions presented in Figure 8, we set $\epsilon = 0.016$, $h = 0.04$, $\sigma = \frac{1}{4}$, and $\omega = 0.075$.

In Figure 9, we present droplet assemblies with $n_b = 2, 3, 6, 8, 12, 20$; $a = 9$ in Figure 9(a) and (b), $a = 6$ in Figure 9(c)–(g), (i)–(j), and $a = 3$ in Figure 9(h). Figures 9(a)–(j) are consistent with the droplet locations based on the sharp interface model. Figure 9(g) is interesting, because it appears there are two different droplet sizes in the same assembly.

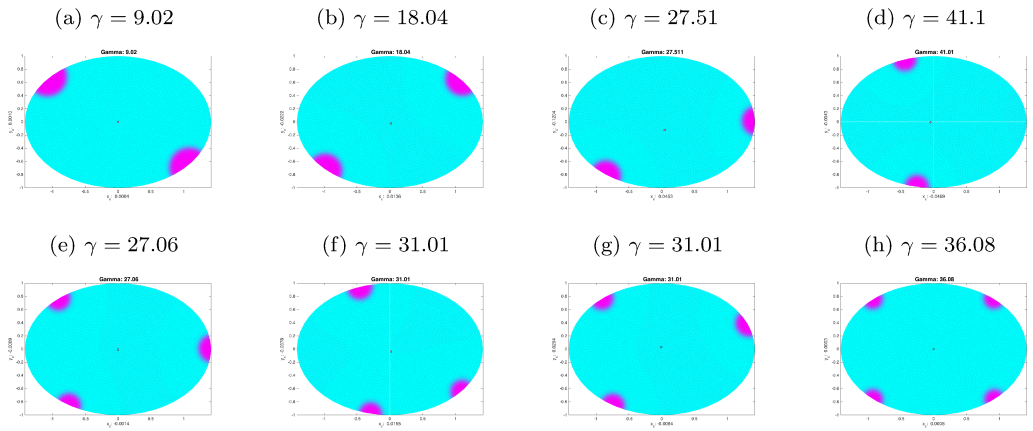

Figure 8. *Boundary droplet assemblies* $n_b = 2, 3, 4$.

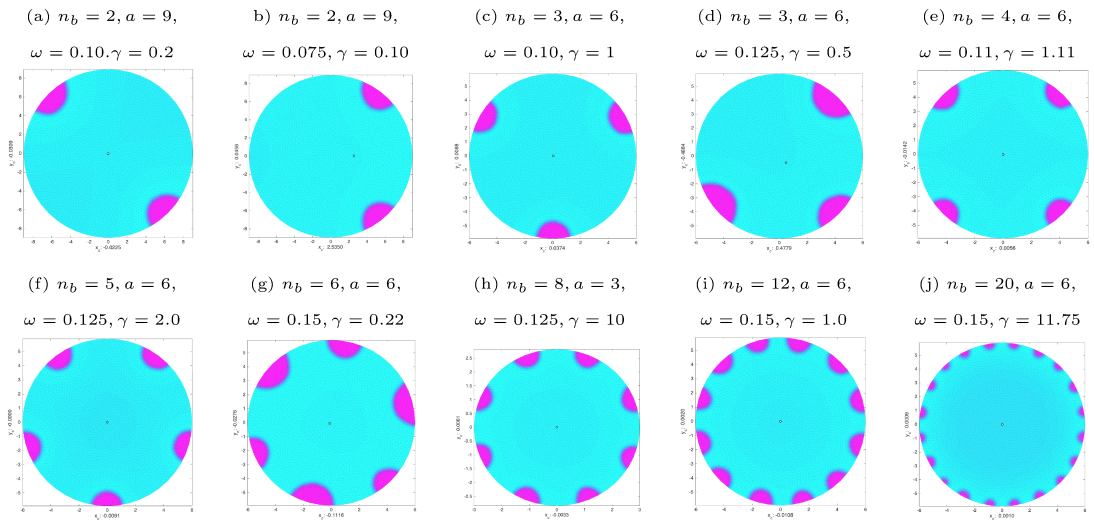

Figure 9. *Droplet assemblies for nearly circular domains;* $n_b = 2, 3, 4, 5, 6, 8, 12, 20$.

5. Concluding remarks. In this paper, we investigate boundary droplet pattern formation in a two-phase system on a two-dimensional manifold. We focus on the case of an ellipse with semimajor axis $a > 1$ and semiminor axis $b = \sqrt{a^2 - 1}$. Based on the analysis of the sharp interface problem, we are able to fully characterize the behavior of a single boundary droplet. When γ is small, the droplet locates to a position $\xi_* = \pm a + 0i$ that maximizes $\kappa(\xi)$, the curvature of the boundary. When $\gamma\rho^2 \to \beta$, the droplet locates to a position that minimizes a linear combination of $\kappa(\xi)$ and $R_b(\xi, \xi)$. For large γ, the droplet locates to a position that minimizes R_b. R_b has two local minima located at $\xi \approx 0 \pm ib$ where κ is also minimized. We are able to fully characterize the behavior of a boundary droplet assembly with $n_b = 2$, but the combinatorics of droplet location are complicated for assemblies where n_b is large. In general, there are numerous local minima and a numerical solution depends on a and γ as well as the initial configuration of the assembly. Nevertheless, numerical solutions of the diffuse interface problem of the Ohta–Kawasaki model were consistent with predictions based on the sharp interface model. Using finite element solutions, we confirm the behavior of a single boundary droplet. In addition, we compute droplet assemblies with $2 \le n_b \le 20$. In a boundary droplet assembly with six droplets, numerical evidence suggests a local minimum with two distinct droplet sizes. The droplets are arranged along the perimeter with the droplets alternating in size. In future work, we plan to extend our analysis to include both interior droplets and boundary droplets.

Appendix A. Conformal map of an ellipse to the unit disk. Consider the problem of conformally mapping an ellipse

$$\mathbb{E}_{a,b} = \left\{(x, y) \mid (x/a)^2 + (y/b)^2 < 1\right\} \tag{41}$$

onto the unit disk

$$\mathbb{D} = \left\{(u, v) \mid u^2 + v^2 < 1\right\}.$$

Without loss of generality, we can assume $a > 1$ and $b^2 = a^2 - 1$ and, in this case, denote the ellipse by $\mathbb{E}_a$. The solution to this conformal mapping problem is well known (see, e.g., [6, 11, 22]). However, [6, 11] contain misprints and [22] requires some additional background for our application. For these reasons, we present a self-contained exposition here.

Let $-\frac{1}{2}\pi < \xi_1 < \frac{1}{2}\pi$ and $0 < \xi_2 < c$, where $c = \cosh^{-1}(a)$ and $b = \sinh c$. The *period rectangle* $\mathcal{R}$ is

$$\mathcal{R} = \left\{\xi = \xi_1 + i\xi_2 \ \mid -\tfrac{1}{2}\pi < \mathrm{Re}(\xi) < \tfrac{1}{2}\pi, 0 < \mathrm{Im}(\xi) < c\right\}$$

(see Figure 10(a)). By construction, $z = \sin\xi$ maps $\xi \in \mathcal{R}$ to $z \in \mathbb{E}_a$ with $a = \cosh c$ and $b = \sinh c$, i.e.,

$$z = x + iy = \sin(\xi_1 + i\xi_2) = \sin\xi_1 \cosh\xi_2 + i\cos\xi_1 \sinh\xi_2 \tag{42}$$

and

$$\left(\frac{x}{\cosh\xi_2}\right)^2 + \left(\frac{y}{\sinh\xi_2}\right)^2 = 1, \quad 1 \le \cosh\xi_2 \le \cosh c.$$

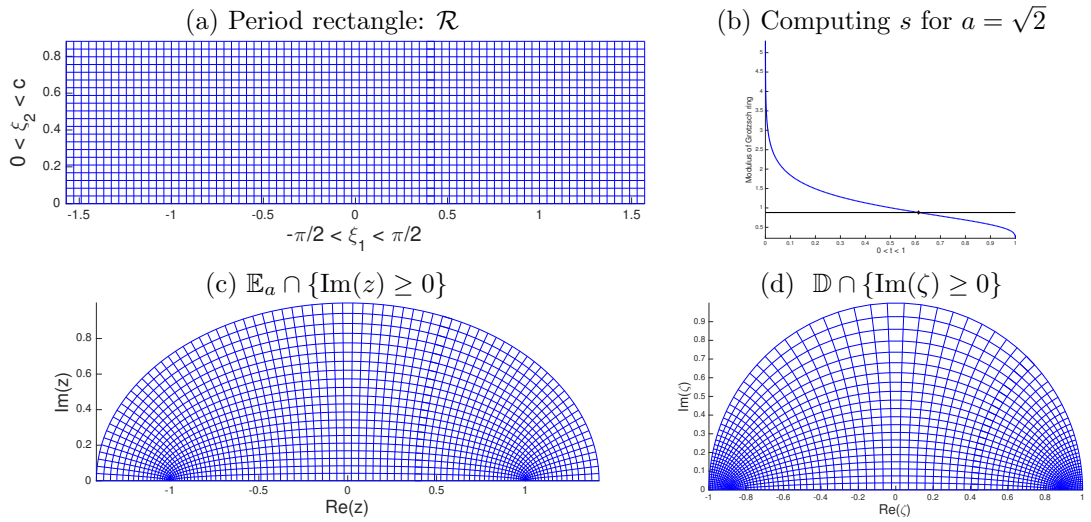

Figure 10. *For $a = \sqrt{2}$:* (a) *period rectangle $\mathcal{R}$;* (b) *intersection of $y = \frac{1}{2}\pi \mathsf{K}'(t^2)/\mathsf{K}(t^2), t \in (0,1)$ and $y = \cosh^{-1} a$;* (c) $\mathbb{E}_a \cap \{Im(z) \geq 0\}$; (d) $\mathbb{D} \cap \{Im(\zeta) \geq 0\}$.

When $\xi_2 = 0$ and $y = 0$, the ellipse is degenerate, and the parametrization covers the segment $-\cosh c \leq x \leq \cosh c$ two times. Orthogonal to this family of ellipses is the family of hyperbolas,

$$\left(\frac{x}{\sin \xi_1}\right)^2 - \left(\frac{y}{\cos \xi_1}\right)^2 = 1, \quad -\tfrac{1}{2}\pi < \xi_1 < \tfrac{1}{2}\pi.$$

The boundary of an ellipse is parametrized by setting $\xi_2 = c$ and extending ξ_1 to the interval $-\frac{1}{2}\pi < \xi_1 < \frac{3}{2}\pi$.

Jacobi elliptic functions will be used to define the desired conformal map from $\mathbb{E}_a$ to $\mathbb{D}$. The Jacobi elliptic functions $\mathrm{sn}, \mathrm{cn}, \mathrm{dn}$ can be defined by certain integrals involving a parameter m (see [1, Chap. 16–17]). The modulus of the Jacobi elliptic functions is denoted by k, where $k^2 = m$. In our application, m is real and $0 \leq m \leq 1$. In particular, if

$$u(\phi|m) := \int_0^\phi \frac{d\theta}{\sqrt{1 - m \sin^2 \phi}},$$

we define

$$\mathrm{sn}u = \mathrm{sn}(u|m) = \sin(\phi|m), \quad \mathrm{cn}(u) = \mathrm{cn}(u|m) = \cos(\phi|m), \quad \mathrm{dn}(u|m) = (1 - m \sin^2 \phi)^{1/2}.$$

Dependence on m is denoted by a vertical slash preceding the parameter m. When the value of the parameter is clear from context, m is sometimes suppressed. The real quarter period of the Jacobi elliptic functions is denoted by $\mathsf{K}(m)$, where

$$\mathsf{K}(m) = \int_0^1 \frac{dx}{\sqrt{(1 - x^2)(1 - mx^2)}}.$$

Following the approach in [6], we define the imaginary quarter period of the corresponding Jacobi elliptic functions to be $i\mathsf{K}'(m)$, where

$$\mathsf{K}'(m) := \tfrac{1}{2}\mathsf{K}(1-m),$$

and seek to determine the value t satisfying the equation

$$\frac{\pi}{2}\frac{\mathsf{K}'(t^2)}{\mathsf{K}(t^2)} = c, \quad 0 < t < 1. \tag{43}$$

The quantity $\frac{\pi}{2}\frac{\mathsf{K}'}{\mathsf{K}}$ is known as the modulus of the Grötzsch ring and the related quantity $q = \exp(-\pi\mathsf{K}'/\mathsf{K})$ is called the *nome*. In Figure 10(b), we plot the function $y = \frac{1}{2}\pi\mathsf{K}'(t^2)/\mathsf{K}(t^2)$ for $0 < t < 1$ and show its intersection with the line $y = c$, where $c = \cosh^{-1}(a)$ and $a = \sqrt{2}$. If the solution of (43) is denoted by $t = s$, we define

$$K = \mathsf{K}(s^2) \quad \text{and} \quad K' = \tfrac{1}{2}\mathsf{K}(1-s^2). \tag{44}$$

In Figure 10(c) we present the upper half of $\mathbb{E}_a$ with $a = \sqrt{2}$. Figure 10(d) shows the upper half of $\mathbb{D}$. Although the ellipse is cut from $-1+0i$ to $1+0i$ on the real axis, the maps under consideration can be analytically continued across the real axis by the Schwartz reflection principle.

Since $\pi K'/(2cK) = 1$ for $z \in \mathbb{E}_a$,

$$\arcsin z = \xi_1 + i\xi_2, \tag{45}$$

$$\frac{2K}{\pi}\arcsin z = \frac{2K}{\pi}\xi_1 + i\frac{2K}{\pi}\left(\frac{\pi}{2c}\frac{K'}{K}\right)\xi_2, \tag{46}$$

and it follows that

$$\begin{aligned}
\operatorname{Re}\left(\frac{2K}{\pi}\arcsin z\right) &= \frac{2K}{\pi}\xi_1 \in (-K, K),\\
\operatorname{Im}\left(\frac{2K}{\pi}\arcsin z\right) &= \frac{2K'}{c\pi}\xi_2 \in (0, K').
\end{aligned}$$

The desired conformal map from $z \in \mathbb{E}_a$ to $\zeta \in \mathbb{D}$ is

$$\zeta = \left(\sqrt[4]{s}\right)\operatorname{sn}\left(\left(\frac{2K}{\pi}\arcsin z\right)\middle| s\right), \tag{47}$$

where $t = s$ denotes the solution of (43) and $K = \mathsf{K}(s^2)$ is defined in (44). When $z = \pm 1$, we find $\zeta = \pm s^{1/4}$, respectively. The image of the upper half of $\mathbb{E}_a$ is the upper half of the unit disk $\mathbb{D}$, as shown in Figure 10(d). Equation (47) is in agreement with [11, eq. (51)].

From (45) and (46), we set $\tau := u + iv = \frac{2K}{\pi}\arcsin z$. Hence,

$$u = \frac{2K}{\pi}\xi_1 \in (-K, K) \tag{48}$$

and $v = \frac{K'}{c}\xi_2 \in (0, K')$. Setting $\xi_2 = c$ in (42), we can parametrize $\partial\mathbb{E}_a$ in terms of u which leads to

$$z = x + iy = a\mathrm{sn}(u) + ib\mathrm{cn}(u) \quad \text{for} \quad -K < u < 3K,$$

or any interval of length $4K$. The boundary curvature of $\mathbb{E}_{a,b}$ (see (41)) is

$$\kappa(x,y) = \frac{ab}{((bx/a)^2 + (ay/b)^2)^{3/2}}, \ (x,y) \in \partial\mathbb{E}_{a,b}, \tag{49}$$

$\kappa(\pm a, 0) = a/b^2$, and $\kappa(0, \pm b) = b/a^2$.

Acknowledgments. The authors are grateful to the reviewers whose comments helped to improve the exposition in the paper. The authors are also grateful to Valerio Batista-Ramos for clarifying the definition of the modulus s in Appendix A. The authors acknowledge the Colonial One high-performance computing resource at The George Washington University.

REFERENCES

[1] I. Abramowitz and M. Stegun, *Handbook of Mathematical Functions*, Dover, New York, 1972.
[2] T. Aubin, *Nonlinear Analysis on Manifolds. Monge-Amperé Equations*, Springer-Verlag, New York, 1980.
[3] X. Chen and Y. Oshita, *Periodicity and uniqueness of global minimizers of an energy functional containing a long-range interaction*, SIAM J. Math. Anal., 37 (2005), pp. 1299–1332, https://doi.org/10.1137/S0036141004441155.
[4] R. Choksi and X. Ren, *On the derivation of a density functional theory for microphase separation of diblock copolymers*, J. Stat. Phys., 113 (2003), pp. 151–176.
[5] Y. Hu, *Disc Assemblies and Spike Assemblies in Inhibitory Systems*, Ph.D. thesis, Department of Mathematics, George Washington University, 2016.
[6] S. Kanas and T. Sugawa, *On conformal representations of the interior of an ellipse*, Ann. Acad. Sci. Fenn. Math., 31 (2006), pp. 329–348.
[7] A. Karageorghis and Y.-S. Smyrlis, *Conformal mapping for the efficient mfs solution of Dirichlet boundary value problems*, Computing, 83 (2008), pp. 1–24.
[8] K. Kawasaki, T. Ohta, and M. Kohrogui, *Equilibrium morphology of block copolymer melts.* 2, Macromolecules, 21 (1988), pp. 2972–2980, https://doi.org/10.1021/ma00188a014.
[9] S. Larsson and V. Thomée, *Partial Differential Equations with Numerical Methods*, Springer-Verlag, Berlin, Heidelberg, New York, 2003.
[10] C. B. Muratov, *Theory of domain patterns in systems with long-range interactions of coulomb type*, Phys. Rev. E, 66 (2002), pp. 66–108.
[11] Z. Nehari, *Conformal Mapping*, Dover, New York, 1975.
[12] K. J. Nurmela, *Minimum-energy point charge configurations on a circular disk*, J. Phys. A, 31 (1998), p. 1035.
[13] T. Ohta and K. Kawasaki, *Equilibrium morphology of block copolymer melts*, Macromolecules, 19 (1986), pp. 2621–2632, https://doi.org/10.1021/ma00164a028.
[14] P. O. Persson and G. Strang, *A simple mesh generator in MATLAB*, SIAM Rev., 46 (2004), pp. 329–345.
[15] X. Ren and D. Shoup, *The impact of the domain boundary on an inhibitory system: Existence and location of a stationary half disc*, Comm. Math. Phys., 340 (2015), pp. 355–412, https://doi.org/10.1007/s00220-015-2451-4.
[16] X. Ren and J. Wei, *On energy minimzers of the diblock copolymer problem*, Interfaces Free Bound. 5 (2003), pp. 193–238, https://doi.org/10.1007/s00220-015-2451-4.
[17] X. Ren and J. Wei, *Wriggled lamellar solutions and their stability in the diblock copolymer problem*, SIAM J. Math. Anal., 37 (2005), pp. 455–489, https://doi.org/10.1137/S0036141003433589.

[18] X. Ren and J. Wei, *Many droplet pattern in the cylindrical phase of diblock copolymer morphology*, Rev. Math. Phys., 19 (2007), pp. 879–921.
[19] X. Ren and J. Wei, *Oval shaped droplet solutions in the saturation process of some pattern formation problems*, SIAM J. Appl. Math., 70 (2009), pp. 1120–1138, https://doi.org/10.1137/080742361.
[20] D. Shoup, *Half Disc Sets on the Boundary of a Binary Inhibitory System*, Ph.D. thesis, Department of Mathematics, George Washington University, 2015.
[21] P. Sternberg and I. Topaloglu, *On the global minimizers of a nonlocal isoperimetric problem in two dimensions*, Interfaces Free Bound., 13 (2011), pp. 155–169.
[22] G. Szego, *Conformal mapping of the interior of an ellipse onto a circle*, Amer. Math. Monthly, 57 (1950), pp. 474–478.
[23] I. Topaloglu, *On a nonlocal isoperimetric problem on the two-sphere*, Comm. Pure Appl. Math., 12 (2013), pp. 597–620.
[24] H. F. Weinberger, *A First Course in Partial Differential Equations with Complex Variables and Transform Methods*, Dover, New York, 1965.